Journal Name

ARTICLE TYPE

Cite this: DOI: 10.1039/xxxxxxxxxx

Controlled production of sub-millimeter liquid core hydrogel capsules for parallelized 3D cell culture

Hugo Doméjean,[a] Mathieu de la Motte Saint Pierre,[a] Anette Funfak,[a] Nicolas Atrux-Tallau,[a] Kevin Alessandri,[b,c] Pierre Nassoy,[b,c] Jérôme Bibette,[a] and Nicolas Bremond *a†

Received Date
Accepted Date

DOI: 10.1039/xxxxxxxxxx

www.rsc.org/journalname

Liquid core capsules having a hydrogel membrane are becoming a versatile tool for three-dimensional culture of micro-organisms and mammalian cells. Making sub-millimeter capsules at a high rate, *via* the breakup of a compound jet in air, opens the way to high throughput screening applications. However, a control of the capsule size monodispersity, especially required for quantitative bioassays, was still lacking. Here, we report how the understanding of the underlying hydrodynamic instabilities that occur during the process can lead to calibrated core-shell bioreactors. This implies: i) to damp the shear layer instability that develops inside the injector arising from the co-annular flow configuration of liquid phases having contrasted viscoelastic properties; ii) to control the capillary instability of the compound jet by superposing a harmonic perturbation to the shell flow; iii) to avoid coalescence of drop during jet fragmentation as well as during drop flight towards the gelling bath, and iv) to ensure a proper engulfment of the compound drops into the gelling bath for building a closed hydrogel shell. We end up with the creation of numerous identical compartments in which cells are able to form mutlicellular aggregates, namely spheroids. In addition, we implement an intermediate composite hydrogel layer, composed of alginate and collagen, allowing cell adhesion and thus the formation of epithelia or monolayers of cells.

1 Introduction

The ongoing development of three-dimensional (3D) cell culture techniques enables to better recapitulate *in-vivo* conditions which are needed for recovering the proper cellular function as compared to two-dimensional culture methods [1]. The applications of such approaches range from fundamental biological questions [2] to tissue engineering [3] or drug development and discovery [4]. For example, spheroids, i.e. multicellular aggregates formed by aggregation or proliferation from scaffold free methods [5], has become a popular model in cancer research [6,7]. Despite numerous strategies of 3D cell culture, a standardized method that would allow high throughput screening, easy manipulation of the micro-tissues having controlled and reproducible features is still lacking and is thus a field of intense investigations [8].

The encapsulation of cells in hydrogel-based compartments is a promising way towards this goal [9,10]. Indeed, hydrogels offer to the cells a physical barrier against any mechanical stress during manipulation but also against host immune response for in-vivo delivery applications [11]. In addition, the fabrication methods of such bioreactors rely on the formation of liquid droplets, either by emulsification [12] or by atomization [13], which can be often massively produced. However, the entrapment of cells in a polymer matrix inhibit cell-cell interactions which are crucial for recapitulating proper cell functions of cells forming tissues, like epithelia, or organs. Various strategies have been then developed for creating liquid core capsules where cells can aggregate and form micro-tissues. This includes the deposition of polyelectrolyte layers on a gelled core that is further liquified [14–16], by diffusion of

[a] *Laboratoire Colloïdes et Matériaux Divisés, CNRS, Chemistry Biology & Innovation, ESPCI Paris, PSL Research University, 10 rue Vauquelin, F-75005 Paris, France. E-mail: nicolas.bremond@espci.fr*
[b] *Université de Bordeaux, LP2N, F-33400 Talence, France.*
[c] *Institut d'Optique & CNRS, LP2N, UMR 5298, F-33400 Talence, France.*
† Electronic Supplementary Information (ESI) available. See DOI: 10.1039/b000000x/

the gelling agent towards the core of the drop containing the polymers with a precise control of the reaction time that sets the shell thickness[17], and finally by gelling the outer layer of a compound drop[18]. Compound drops are usually obtained by a co-extrusion technique[19] where electric field can be used to further decrease capsule size[20,21].
Another key feature for achieving an efficient bioreactor for 3D cell culture is a control of capsule size homogeneity. When using an atomization step, monodisperse capsules can be realized by controlling compound jet fragmentation by imposing harmonic vibrations[22–24]. Calibrated hydrogel compartments can also be obtained by using an emulsification strategy combined with microfluidic techniques[25–30]. Core-shell objects can then be produced with three-dimensional co-flow microsystems[31,32] or *via* water-water-oil double emulsions[33].

Recently, we proposed a process for making capsules having a thin alginate hydrogel membrane and an aqueous core[34]. The method relies on a co-extrusion step in air followed by a sol-gel transition of the shell in a gelling bath and does not require the use of any organic phase, in contrast to emulsification-based strategies. Robust formation of capsules having a thin hydrogel membrane is obtained by precisely controlling the physicochemical properties of liquid interfaces. Capsule size varies from a few millimeters, when compound drops are made in a dripping mode[34], down to a few hundreds of micrometers in a jetting mode[35]. As demonstrated for micro-organisms[34] and for the formation of mammalian cell aggregates[35], it is a promising tool for cell culture. Major advantages of this process is first to involve only biocompatible aqueous solutions, which makes easier further manipulation that can be done with classical pipetting techniques. Indeed, the hydrogel shell offers a mechanical protection to the cells but also prevents any adhesion between micro-tissues during culture. Finally, its high production rate, of the order of 1 kHz, opens the way to high throughput applications. However, a control of the capsule size monodispersity resulting from the fragmentation of a compound jet, especially required for quantitative bioassays, is still lacking. Indeed, without any control of the compound jet fragmentation, the coefficient of variation of the capsule size is about 25 %[35].

In this article, we report in detail how the understanding of the underlying hydrodynamic instabilities arising during the process makes possible the creation of calibrated core-shell bioreactors. We demonstrate that it is then possible to create numerous identical compartments where cells are able to grow and to form spheroids. In addition, we implement an intermediate composite hydrogel layer, composed of alginate and collagen, allowing cell adhesion and thus the formation of epithelia.

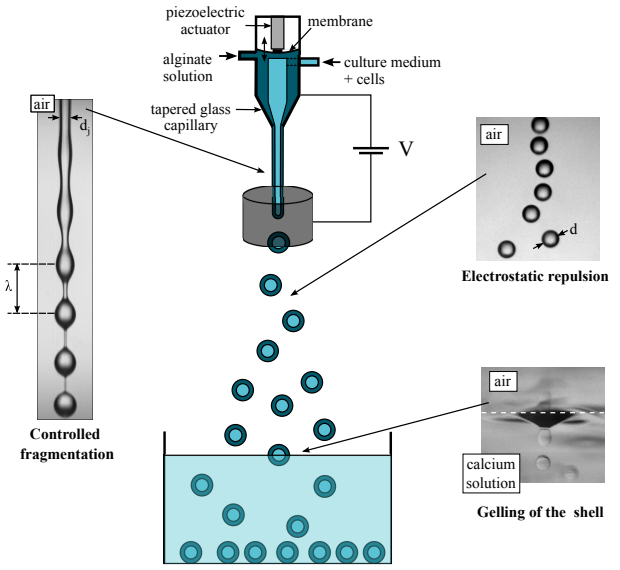

Fig. 1 Work flow of the process for creating calibrated sub-millimeter liquid core hydrogel capsules.

2 Results and Discussion

2.1 Working principle of the encapsulation method

The basic principle of the capsule formation implies a co-extrusion step in air, followed by a fragmentation step and finally a gelling step of the resulting compound drops in an aqueous bath. Since all liquid phases are aqueous solutions, mixing should be suppressed. This is achieved by adding surfactants into the outer polymer solution and the gelling bath that favor a proper engulfing of the compound drop and thus a homogeneous sol-gel transition of the alginate layer[34]. Depending on the flow rates of the different liquid phases, and thus on liquid inertia, drops are either formed in a dripping regime or a jetting one[36]. In the dripping regime, since drop formation is the result of a competition between gravity and surface tension, the drop diameter d varies like $d_o^{1/3}$ for low liquid flow rate and small outer diameter d_o of the tube from which liquids exit[37]. Although this process gives rise to perfectly monodisperse drops and thus capsules, it is thus difficult to create sub-millimeter drops. One option to further decrease drop size is to shear off the pending drops attached to the nozzle with the help of an air co-flow[38]. An alternative way is to increase fluid inertia in order to form a jet whose fragmentation under capillary instability leads to drop size that scales with the jet size itself[39]. This strategy, which has been previously used[35], is also followed in the present work but with a better control.

The working principle of the sub-millimeter capsule formation process is reported in Figure 1. A compound jet is generated by a co-axial injector, made by stereolithography technique, terminated by a tapered glass capillary whose inner diameter d_i is 150

μm for most of the reported experiments, or 170 μm. The outer liquid is an alginate solution. It flows through a chamber where an elastic membrane is subjected to harmonic vibrations with the help of a piezoelectric actuator[23]. In that way, the capillary instability is forced at a controlled wavelength λ[40]. By mass conservation and for monodisperse drops, the drop diameter d is equal to $(3/2d_j^2\lambda)^{1/3}$, where d_j is the jet diameter. The shell thickness h is tuned by the flow rate ratio $r_q = q_i/q_o$, where q_i and q_o are the flow rates of the inner phase and the outer phase, respectively. Indeed, by mass conservation, $h = d/2(1-(r_q/(1+r_q))^{1/3})$. As originally proposed by Brandenberger *et al.*[41], eventual coalescence of drops while they are flying to or entering into the gelling bath is prevented by electrically charging the drops. This is achieved by adding an electrode at the location of the jet break-up and set at a potential of the order of 1 kV while grounding the alginate solution. The drops then gain a net electric charge[42] and repulse each other before impacting the gelling bath where the outer alginate layer turns into gel.

2.2 Compound jet formation and fragmentation

Before discussing on the compound jet breakup, let us focus on the formation of the jet itself. As reported in Figure 2 and in Movie S1[†], the jet exhibits a flapping motion whose amplitude depends on the liquid phase composition and flow rate ratio. The oscillatory motion of the jet is here characterized by the standard deviation σ_{y_c} of the jet's center location y_c. All reported data have been taken at a distance x_c from the capillary tip around 3 mm. For a core only composed of water, the jet moderately beats up to an amplitude of 10 μm for large flow rate ratio. On the other hand, we observe a marked flapping motion with an amplitude of a few tens of μm once NaCl is added into the core solution. The undulations of the jet can be damped if a polymer, here HydroxyEthylCellulose (HEC), is also added into the core solution. Indeed, σ_{y_c} is almost not measurable for an HEC concentration of 0.5 wt% that corresponds to the most viscous condition (see Table 2).

Flapping can thus be attenuated but we may wonder what is the origin of such a behavior. As revealed by the snapshots shown in Figure 2, the co-flow inside the injector also exhibits a non-stationnary feature, i.e. the core center location is oscillating. This motion is the signature of a viscoelastic shear instability triggered by the contrast of viscoelastic properties between the core and the shell solutions[43,44]. In addition, the observed spiral motion, that corresponds to a non-axysimmetric mode, has been predicted to be the most unstable one[43]. The remarkable effect of NaCl is linked to the nature of alginate which is a polyelectrolyte, i.e. an ionic polymer. Indeed, the presence of ions in solution screens electrostatic repulsion between polymer chains that affects the entanglement conformation of the polymer and thus the rheological properties of the solution[45]. This is confirmed by oscillatory rheological measurements where $\tan\delta$, which is the ratio between the viscous and the elastic moduli[46], varies from 12.9 to 6 at a pulsation of 1 rad.s^{-1} when 75 mM of NaCl is incorporated into the alginate solution. This difference persists at a higher pulsation of 100 rad.s^{-1} where $\tan\delta$ is equal to 1.5 and 1.3 without and with salt, respectively. We note that the viscoelastic instability of the co-flow is here triggered at the interface between the core and the shell by diffusion of ions from the core. Fortunately, this shear instability is damped by increasing the core viscosity by adding a small amount of a non gelling polymer. This flapping motion has a direct impact on the efficiency of capsule formation as discussed in the next section.

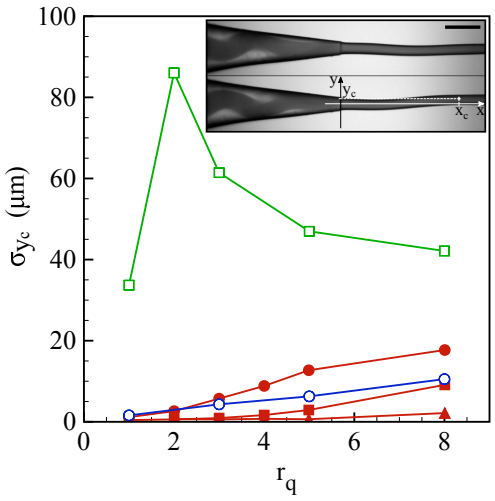

Fig. 2 Transversal fluctuation σ_{y_c} of the jet's center location y_c as a function of the flow rate ratio r_q for three core compositions: water (○), water with 75 mM NaCl (□), water with 75 mM NaCl and 0.14 wt% HEC (●), 0.25 wt% HEC (■) and 0.5 wt% HEC (▲). Inset: two snapshots showing compound jet flapping along with axes and jet's center location. For visualization purpose, ink is incorporated into the core solution. The core exhibits a spiraling motion inside the glass tip visible on the left hand side. The scale bar is 500 μm.

Another consequence of such a non-newtonian behavior is the increase of the jet diameter as compared to the inner injector one. This phenomenon, known as die-swelling, is linked to normal stresses built within the injector that relax within the free jet and slows down the flow[47,48]. We note that jet swelling may also result from viscous stress relaxation[49]. The jet diameter increase is accentuated for thick alginate layers, i.e. for small flow rate ratios r_q. Indeed, for a core having a viscosity of 34 mPa.s, an alginate solution (LF200FTS) at a concentration of 1.7 wt% and for a total flow rate of 120 mL/h, the jet diameter d_j varies from 1.2 times d_i to 1.5 times d_i when r_q is tuned from 10 to 0. As previously discussed, this has a direct impact on final capsule size since it is correlated to jet size.

The atomization of the compound jet when the primary vis-

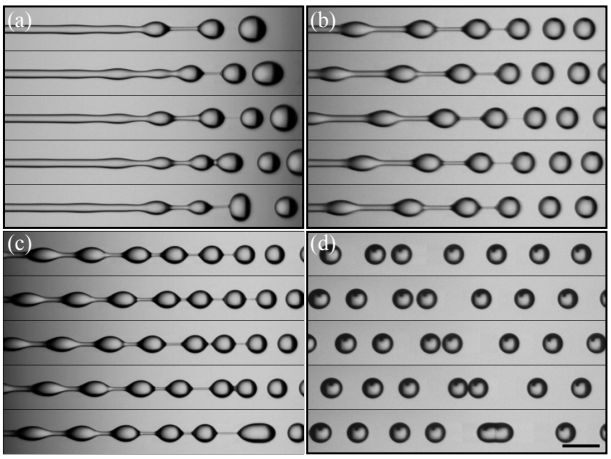

Fig. 3 Time sequences showing the fragmentation of a free compound jet (a), a regular breakup of a jet under harmonic perturbations (b) and drop coalescence among the jet (c) or in flight (d) due to velocity fluctuations that lead to capsule size polydispersity. The time step between two consecutive snapshots is 1 ms and the scale bar is 1 mm.

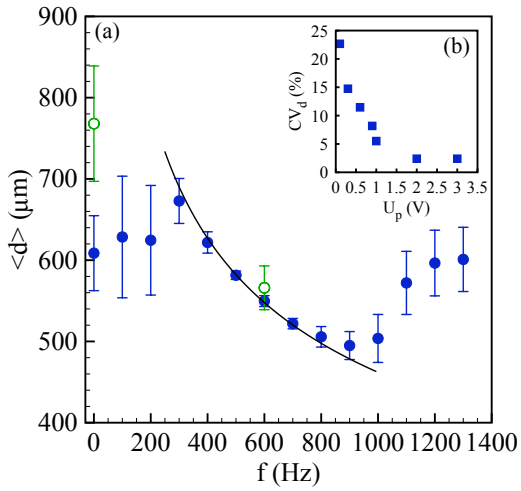

Fig. 4 (a) Evolution of the average compound drop size $< d >$ with the frequency f imposed to the piezoelectric actuator in presence of the electric field (●) and without (○). The continuous line represents a power law of $-1/3$, as expected from mass conservation and for monodisperse drops. The voltage U_p applied to the piezoelectric actuator is 3 V. (b) Evolution of the coefficient of variation of the compound drop size CV_d, defined by the ratio between the standard deviation of the drop size and the mean size, with the voltage U_p for $f = 600$ Hz. For both set of experiments, the inner diameter of the glass tip is 170 μm, the flow rate ratio is 3, the total flow rate is 140 mL/h, the outer solution viscosity is 1.82 Pa.s and the inner one is 51 mPa.s.

coelastic instability is damped is now investigated. Time sequences showing the jet fragmentation are reported in Figure 3. In absence of any external forcing, several wavelengths are developing along the jet and thus lead to heterogeneous drop size (Figure 3 (a), Movie S2[†]). Imposing flow rate modulations, with the help of a piezoelectric actuator, then allows to select a specific wavelength and thus to obtain a monodisperse train of drops (Figure 3 (b)). We note that drops are connected by cylindrical liquid filaments, thus forming a drops on a string structure. The radius of the liquid bridge linearly decreases with time until it ruptures[50]. This is reminiscent of the pinch-off of a viscous liquid cylinder[39]. Despite controlled perturbations, we observe the occurence of drop coalescence either during the jet fragmentation (Figure 3 (c)) or after breakup (Figure 3 (d)) that ultimately lead to size polydispersity. A representative high speed recording of such phenomena is shown in Movie S3[†]. The origin of such coalescence events is linked to the spatial feature of the capillary instability where capillary and viscous forces acting on the drops evolve along the jet and ultimately amplify small velocity fluctuations. Such velocity fluctuations are linked to the unstable nature of the annular co-flow of liquids having contrasted viscoelastic properties[43,44]. More details about this unstable fragmentation can be found elsewhere[50].

Since the growth rate of the capillary instability depends on the wavenumber $k = 2\pi/\lambda$ in a non-monotonic way, with a maximum and a cut-off wavenumber equal to $1/d_j$, the controlled perturbations features must be set with care[39]. Here, we tune the frequency f and the voltage U_p applied to the piezoelectric component that imposes periodic oscillations of an elastic membrane that finally modulate velocity of the alginate solution. Since the capillary instability is a convective instability, i.e. the waves travel at the fluid velocity u, the selected wavenumber is linked to the frequency by $k = 2\pi f/u$. As a consequence, for a given flow rates condition, the spray characteristics depend on f and U_p. For a single frequency breakup, the drop size should be related to the frequency in such a way: $d = (3/2d_j^2 u/f)^{1/3}$. The average drop size $< d >$ along with the standard deviation represented by error bars are reported in Figure 4 (a) as a function of the frequency for a constant voltage U_p. For a low frequency, up to 200 Hz, the drop size is rather constant and is largely distributed. Indeed, the coefficient of variation of the drop size CV_d, defined by the ratio between the standard deviation of the drop size σ_d and the mean size, i.e. $CV_d = \sigma_d / < d >$, is more than 15 %. Then the drop size follows the expected power law $f^{-1/3}$ which is valid for monodisperse drops. This criterion is met for a frequency lying between 500 Hz and 700 Hz where CV_d is around 2 %. Then for frequencies larger than 1000 Hz, the average drop size as well as the standard deviation increase and finally saturate. This behavior is a signature of the dispersion relationship of the capillary instability. Indeed, the forcing amplitude is not high enough as compared to the background noise level for being able to select a frequency, and thus a wavenumber, far from the optimal one. This is exemplified in Figure 4 (b) where the drop size variation

is reported as a function of U_p for a fixed frequency. The initial value of CV_d is close to 20 % at $U_p = 0.1$ V and quickly falls down to 5 % at $U_p = 1$ V and saturates around 2 %, i.e. a homogeneous drop size, for U_p larger than 2 V. The drop sizes reported Figure 4 have been measured in presence of an electric field. For comparison, the case without electrically charging the drops is also shown with and without controlled perturbations. The effect of the electric field on avoiding drop coalescence is clearly visible at the optimal frequency equal to 600 Hz where the polydispersity switches from 2 % to 10 % when drops are not electrically charged.

2.3 Encapsulation efficiency

The spray of compound drops then impacts onto the calcium chloride bath that induces a sol-gel transition of the alginate shell. At impact, the drops get flatten while deforming the free interface and a rapid and homogeneous engulfing is required for creating a closed hydrogel shell[34]. We now discuss the influence of the operating conditions on the capsule formation efficiency. The efficiency of encapsulation is assessed by collecting a few hundreds of capsules and by counting the broken capsules (n_b) among intact ones (n_c). The corresponding probability $P_c = n_c/(n_c + n_b)$ to form a capsule is reported in Figure 5 (a) as a function of the core viscosity η_i with and without NaCl for three flow rate ratios, 1, 3 and 5. We notice that P_c is equal to 1 whatever η_i for $r_q = 1$ but the encapsulation fails for small inner fluid viscosity when the flow rate ratio is increased, corresponding to thinner outer layers. The probability to form a capsule is plotted in Figure 5 (b) as a function of the amplitude of lateral jet fluctuations σ_{y_c} as defined in Figure 2. We note that P_c is a linear function of σ_{y_c}, i.e. $P_c = 1 - \alpha\sigma_{y_c}$, where α is equal to 0.63 10^{-2} μm^{-1} and 1.5 10^{-2} μm^{-1} for r_q equal to 3 and 5, respectively. The viscoelastic shear instability that develops inside the injector leads to an off-centering of the core (Figure 2) and thus to a flapping motion of the jet but also to an inhomogeneous alginate layer thickness. Then, the compound drop may burst at impact if the shell thickness is too thin[34]. As a consequence, the probability to form a capsule is directly linked to the amplitude of the lateral jet fluctuations but also to the flow rate ratio that sets the mean shell thickness.

We then wonder what is the value of the critical alginate layer below which encapsulation fails. Experiments are thus performed with a core viscosity such that the jet does not flap anymore. As shown in Figure 6, the critical r_q is between 5 and 8 which corresponds to a critical relative thickness h/d of the outer layer between 0.02 and 0.03. For a compound drop diameter of 500 μm, the critical thickness is then about 12 μm.

We can conclude that the probability to form a capsule is governed by a critical shell thickness below which the full gelling of the alginate layer fails, like for millimeter capsules[34]. However, here the critical thickness is either solely set by the flow rate ratio (Figure 6) or also correlated to the viscoelastic shear instability that develops inside the injector (Figure 2) that leads to an off centering of the core and thus inhomogeneous shell thickness (Figure 5).

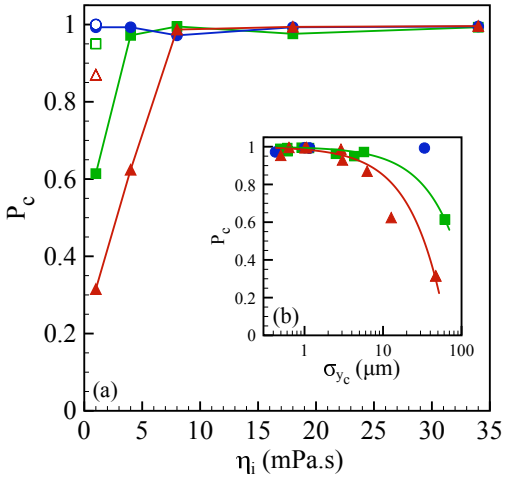

Fig. 5 (a) Probability to form a capsule P_c as a function of the core viscosity η_i in presence of 75 mM NaCl for three flow rate ratios: $r_q = 1$ (●), $r_q = 3$ (■) and $r_q = 5$ (▲); as well as the corresponding probabilities for pure water core (empty symbols). Lines are here to guide the eye. (b) Probability to form a capsule as a function of the transversal fluctuation σ_{y_c} of the jet's center location (see Fig. 2) for three flow rate ratios (same symbols as in (a)). The continuous lines represent a linear fit, $P_c = 1 - \alpha\sigma_{y_c}$, where α is equal to 0.63 10^{-2} μm^{-1} and 1.5 10^{-2} μm^{-1} for r_q equal to 3 and 5, respectively.

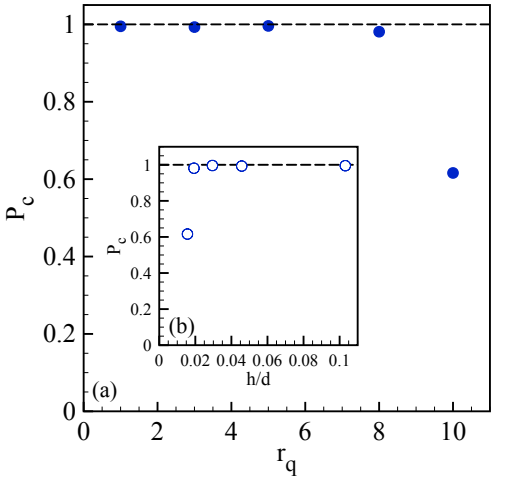

Fig. 6 (a) Probability to form a capsule P_c as a function of the flow rate ratio r_q and with a shell viscosity η_o of 1.82 Pa.s and a core viscosity η_i of 34 mPas. (b) P_c as a function of the relative outer layer thickness h/d. Here, the core is centered since the jet does not flap.

Table 1 Probability to form a capsule P_c for a flow rate ratio of 5 as a function of SDS and $CaCl_2$ concentrations and shell viscosity η_o.

η_o (Pa.s)	η_i (mPa.s)	SDS (mM)	$CaCl_2$ (wt%)	P_c
0.12	34	0.5	1	0.49
0.16	34	0.5	1	0.70
0.44	34	0.5	1	0.94
0.57	34	0.5	1	0.89
1.00	34	0.5	1	0.91
1.82	34	0.5	1	>0.99
1.94	34	0.5	1	>0.99
1.82	51	0.1	1	0
1.82	51	0.25	1	0
1.82	51	0.5	1	>0.99
1.82	51	1	1	>0.99
1.82	51	0.5	0.1	49
1.82	51	0.5	0.5	84
1.82	51	0.5	1	>0.99
1.82	51	0.5	2.5	>0.99

The outer solution viscosity also impacts on the encapsulation efficiency. An alginate having a lower molecular weight in order to be able to vary the solution viscosity by changing the concentration while being above the gelling concentration which is about 1 wt%[51]. The core viscosity is such that the viscoelastic shear instability is damped i.e. the core of the compound jet is kept centered. The values of P_c are reported in Table 1 for a challenging flow rate ratio of 5, i.e. for a rather thin relative alginate layer. The encapsulation efficiency is rapidly decreasing for lower shell viscosity than the one used in most of the experiments presented in this study and close to 1.8 Pa.s. We assume that the origin of this failure is linked to the higher degree of deformation of the compound drop at the impact. A core having a lower viscosity favors internal mixing and thus erosion of the alginate layer before it turns into gel, which is not the case with an immiscible core[34].

Finally, two other physicochemical parameters, namely the calcium and SDS concentrations, are important to succeed in creating aqueous core hydrogel capsules. The efficiency of the encapsulation process is also reported in Table 1. From these experiments, we can conclude that the minimum SDS concentration is 0.5 mM and the calcium chloride one is 1 wt% that corresponds to 9 mM. Also, traces of surfactant (here tween 20) into the gelling bath should be present for ensuring a proper compound drop engulfing and thus an efficient solidification of the whole shell[34].

2.4 A tool for parallelized 3D cell culture

After having defined the right workflow along with the optimal flow, actuation and physichochemical parameters for making a robust process leading to well calibrated liquid core hydrogel capsules, the process is now confronted to cell culture experiments. We study the encapsulation of CT26 cells, cancer cells from mouse, that are known to aggregate without adhesion on the alginate hydrogel[35]. The core is composed of a cell solution with 0.5 wt% of HEC that corresponds to a core viscosity of 34 mPa.s. The cell concentration is 5×10^5 cells/mL and leads to an initial expected number of encapsulated cells of around 14 per capsule. The flow rate ratio is 2 and the total one is set to 150 mL/h. The optimal frequency of the harmonic forcing is found to be 500 Hz that gives rise to capsule size of the order of 500 μm. Bright field images of a collection of capsules into which cells proliferate are shown in Figures 7 (a,b,c) for different days after encapsulation. At day 1, cells mostly form a single aggregate. Then, the spheroids reach a size of around 200 μm at day 7. The distribution of spheroid diameter d_s at day 7 is reported in Figure 7 (f). It is well described by a normal distribution with an average diameter of 205 μm and a standard deviation equal to 21 μm. The corresponding coefficient of variation is 11 %. This value is comparable to the other protocols of spheroids formation like the hanging drop technique[53], microfabricated wells[54] or droplet based microfluidics[32] that show a CV between 10 and 15 %. All this techniques are based on a compartmentalization step. The variability in spheroid size is principally due to sampling at a low cell concentration that unavoidably leads to statistically distributed initial cell number[52]. The presence of initial cell aggregates can widen size distribution. A way to overcome this size heterogeneity is to sample highly diluted cell suspensions for favoring single cell encapsulation. On the other hand, this leads to empty compartments (capsules, drops, microwells, ...) that impacts on the throughput capabilities. An alternative way is to encapsulate dense cell suspensions since CV is equal to $1/\sqrt{\nu}$ where ν is the average number of cells per compartment. This condition might be relevant for cells having a low proliferation rate. The size of cell aggregates is actually an important factor for cell viability and function since nutrients, oxygen or drugs have to diffuse through all such avascular tissues[3]. Optimal spheroid size then depend on cell type. For example, aggregates of hepatocytes with a diameter of 100 μm has been shown to exhibit maximal activity[55] and viability[56].

The cell viability of this cell line after encapsulation has been previously estimated at 95 %[35]. For spheroids, the use of standard live dead assay combined with epifluorescence microscopy images is rather difficult. First of all, the dye does not penetrate more than a few cell layers, the viability is thus estimated from cells at the periphery of the spheroid. Then, cell counting is not easy with such three-dimensional structure. An example of a confocal image taken at day 7 is shown in Figure 7 (e). At day 7, the relative intensity of the green channel (alive cells) is close to 90 % (Figure S2†). Therefore, as previously demonstrated[35], the compartmentalized cell culture in liquid core hydrogel capsules allows long duration growth of mammalian cells without altering cell viability.

Some cell types, like epithelial cells, require a connection to the extra cellular matrix (ECM) to enable a proper polarization that regulates their function. The adhesion is promoted through cell receptors interaction with specific motifs of its environment

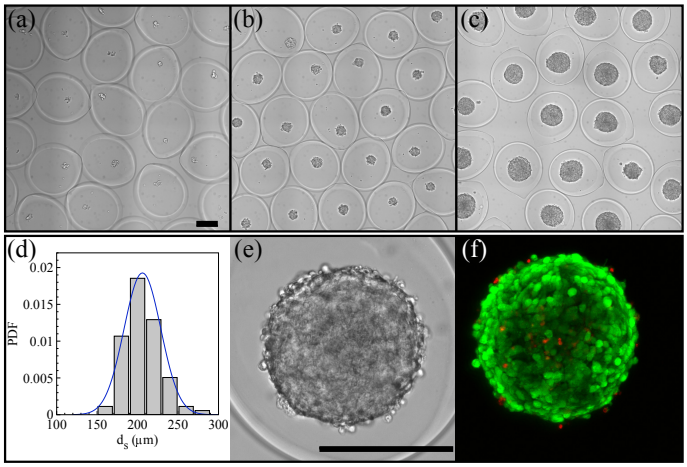

Fig. 7 Formation and growth of CT26 cells spheroids in hydrogel capsules at day 1 after encapsulation (a), day 3 (b) and day 7 (c). (d) Probability density function of the spheroid diameter d_s evaluated from 90 spheroids. The solid line is the adjusted normal distribution with an average diameter of 205 μm and a standard deviation equal to 21 μm. Magnified view of a spheroid (e) along with the z-projection of epifluoresence confocal microscopy image of the spheroid (f) using a live dead assay (dead cells are colored in red). The scale bars are 200 μm.

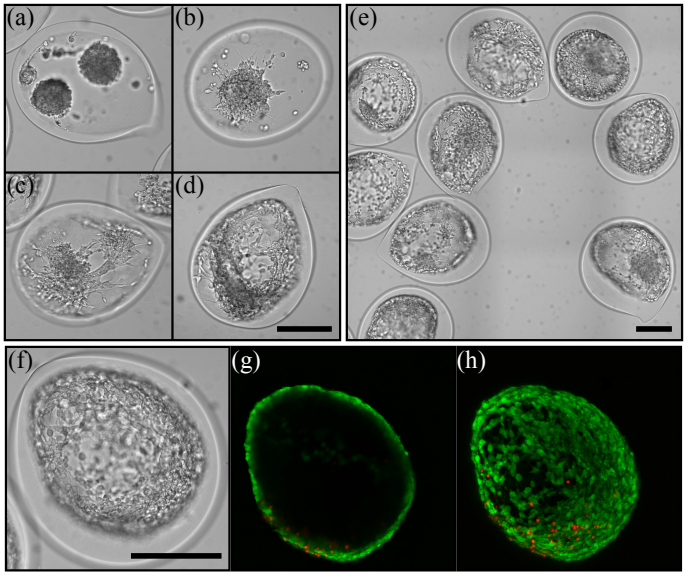

Fig. 8 Encapsulation of CT26 cells in hydrogel capsules having an internal composite hydrogel layer made of alginate-collagen blend for various core to intermediate layer flow rate ratios r_{q2}: 10 (a), 5 (b), 2 (c), 1.25 (d) and 1 (e). The snapshots are taken 9 days after the encapsulation step, excepted for image (e) that corresponds to 7 days of incubation. Magnified view of an adherent monolayer of CT26 cells (f) after 7 days of development on a composite hydrogel for $r_{q2} = 2$. Corresponding epifluorescence confocal microscopy images at the equator of the capsule (g) and the z-projection (h) using a live dead assay. The scale bars are 200 μm.

which are not present in alginate hydrogel. To circumvent this non-adherence feature one can functionalize alginate with peptides[57,58], or by using a polymer blend with proteins extracted from ECM[59] or by an adsorption of proteins on the inner wall of the capsule after encapsulation[60]. In order to make the present bioreactor a more versatile tool for cell culture, an intermediate layer between the core where cells are suspended and the alginate hydrogel membrane is added. The intermediate layer is composed of alginate and collagen type I. Optimal concentrations of collagen and alginate that properly induce cell adhesion have been evaluated with another cell type, keratynocytes[61] (see Material and Methods). Here, we investigate the effect of the flow rate ratio r_{q2} between the core and the intermediate solutions on the ability of cells to spread or not on the inner surface of the capsules. This flow rate ratio sets the average thickness of the composite hydrogel layer but also the homogeneity of the adhesive layer. Indeed, as shown in Figure 8, the flow rate ratio governs the ability of cells to spread on such a substrate. For the highest r_{q2} equal to 10, the loaded cells do not initially aggregate together for building a single spheroid, but multiple spheroids are nucleated instead (Figure 8 (a)). This is a signature of a weak adhesion that contrasts to non adhesive case reported in Figure 7. Then, for a r_{q2} two times lower, multiple spheroids are also observed but in that case some cells at the contact area between the spheroid and the composite substrate exhibit elongated shape (Figure 8 (b)). For r_{q2} equal to or lower than 2, cells adopt an elongated shape and spread out all over the composite hydrogel layer without any preferential location. This clearly indicates the formation of a homogeneous adhesive layer. The area occupied by the cells, that reflects the affinity between the cells and the hybrid hydrogel, shows a marked increase for r_{q2} smaller than 2 (Figure S2†). Confocal microscopy images reported in Figure 8 (g) and (h) illustrate the possibility to form a single cell layer, like simple epithelium. After 7 days of growth inside the structured hydrogel-based bioreactor, the relative intensity of the fluorescent signal from alive cells is around 80 % (Figure S1†).

3 Conclusion

This manuscript reports a methodical study of the process for creating calibrated sub-millimeter liquid core hydrogel capsules that act as bioreactors for 3D cell culture. Let us summarize the key parameters that should be accounted for achieving an efficient cell encapsulation. First, since the capsule formation involve co-flow of polymer solutions, viscoelastic properties of the different solutions should be adapted for avoiding hydrodynamic instabilities. A core viscosity larger than 10 mPa.s is required. This can be obtained by adding a small amount of a non-gelling polymer into the core solution. The amount of cations, either monovalent

or divalent, present in the core solution should be minimized during the encapsulation as they alter the viscoelastic features of the alginate solution. Then, in order to create calibrated capsules, frequency and amplitude of the forcing should be correctly adjusted. Since the capillary instability of the jet exhibits a resonance like behavior, i.e. there exists a most amplified mode, the frequency can be adjusted such that the jet fragmentation length is minimal. However, we recommend to perform a visual inspection of jet fragmentation features with the help of a camera having a fair enough low time exposure, at least 0.1 ms. Finally, a minimal concentration of 0.5 mM of SDS should be added to the alginate solution and a minimal $CaCl_2$ concentration of 1 wt% with traces of surfactant should be used for the gelling bath.

Today, the present technology allows to create calibrated submillimeter compartments enclosing cells at a production rate of the order of 1000 capsules per second. Automated manipulation of the capsules combined with preexisting high throughput technologies, for example based on microplates, would then strengthen the use of the present bioreactor for high throughput screening applications, like drug development or discovery. An adaptation of a millifluidic automate[62,63] initially developed for manipulating emulsion drops into which cells are encapsulated is currently under progress.

4 Material and Methods

4.1 Chemicals

Table 2 Zero shear viscosities η_0 of polymer solutions as a function of the polymer concentration C

Polymer	C (wt%)	η_0 (Pa.s)
LF200FTS	1.7	1.82
LF200S	2	1.70
LF10/60	1.8	0.12
LF10/60	2	0.16
LF10/60	2.5	0.44
LF10/60	3.1	0.57
LF10/60	3.7	1.00
LF10/60	4.7	1.94
HEC	0.14	4×10^{-3}
HEC	0.25	8×10^{-3}
HEC	0.37	18×10^{-3}
HEC	0.50	34×10^{-3}

During the characterization of the capsule formation process, aqueous shell solutions are made with sodium-alginate Protanal LF200FTS, LF200S or LF10/60 (FMC Biopolymer) and Sodium Dodecyl Sulfate (SDS) (Sigma Aldrich), an anionic surfactant. Aqueous core solutions are composed of HydroxyEthylCellulose (HEC) with a mean molecular weight of 1.3 10^6 g.mol^{-1} (Sigma Aldrich) and NaCl (Sigma Aldrich). All polymer solutions are prepared from milliQ water and set under magnetic stirring at least half a day before use. Rheological properties of the solutions are determined with a MCR501 rheometer (Anton Paar) in a Couette geometry or with a ARES LS1 rheometer (TA Instrument) in a cone-plane geometry. For oscillatory measurements, the imposed strain is 1 % and falls into the linear regime. All experiments are performed at 20 °C. Alginate and HEC solutions exhibit a shear-thinning behavior, i.e. viscosity is a decreasing function of the shear rate beyond a critical shear rate. The zero-shear viscosity of the various polymer solutions is in reported Table 2. Gelling baths are $CaCl_2$ (Sigma Aldrich) solutions where a small amount (< 0.1 wt%) of Tween 20 (Sigma Aldrich) is added before starting encapsulation experiments.

4.2 Encapsulation device

The compound jet is created by using a hybrid injector made by stereolithography and glass capillary techniques[64]. A glass capillary with an outer diameter of 1 mm and an inner one of 0.78 mm is first tapered with the help of a gravitational puller (PC-10, Narishige). Then, the tip is cut by using a microforge (M900, Narishige) and finely ground. The final outer and inner diameters are 250 and 150 micrometers, respectively. Some of the experiments, as noticed in the manuscript, are performed with an inner diameter of 170 μm. The surface of the glass tip is made hydrophobic by silanization. The 5 mm long glass tip is glued to a piece made in epoxy by 3D printing (DSM XC11122, Proform) which allows to generate a concentric flow of two or three liquid phases. Before exiting from the glass capillary, the outer liquid flows in a chamber equipped with a membrane (Encapsulator, Bucchi) that can oscillate with the help of a piezoelectric actuator (P-820, PI). Both liquid flows are driven by syringe pumps (PhD Ultra, Harvard Apparatus). The encapsulation device is shown in Figure S3†.

4.3 Encapsulation characterization

The jet is illuminated with a LED panel (SLLUB backlight, Phlox) and observed with a high speed camera (FastCam SA3, Photron) mounted on a macro zoom microscope (MVX10, Olympus) set horizontally. The jet fragmentation features are obtained with image processing programs developed with MATLAB. The encapsulation efficiency is evaluated from image analysis of hundreds of capsules taken under microscope.

4.4 Cell culture

CT26 WT cells (ATCC) are cultured in DMEM, high glucose, GlutaMAX supplement (Life technology) enriched with 10% v/v FBS and 100 units streptomycin/penicillin (10000 units/mL, Life technology) on tissue culture flasks at 37 °C in a humidified 5% CO_2 incubator. After reaching 80% confluence the cells are trypsinized with 0.05% (w/v) Trypsin-EDTA (Life technology), centrifuged at 180 g for 9 min and counted for further experimental use. After the encapsulation step, the hydrogel capsules are washed with

DMEM medium, subsequently transferred in tissue culture flasks and cultivated up to 2 weeks in DMEM, high glucose medium at 37 °C in a humidified 5% CO_2 incubator, followed by a medium change every 2 days.

4.5 Cell encapsulation

The cells are suspended in a solution containing 25 mM of HEPES (Sigma Aldrich) and 265 mM of sorbitol (Sigma Aldrich) and 0.5 wt% of HEC, at a pH of 7.3. Solutions are initially filtered at 0.2 μm. For a single alginate shell, a solution of 2 wt% sodium alginate (LF200S, FCM) containing 0.5 mM SDS and 250 units of streptomycin/penicillin is first filtered with 5 μm sterile filter (VWR) followed by a sterile filtration at 1 μm with a glass filter (Sigma Aldrich).

The collagen alginate mixture is composed of 0.8 wt% of alginate, 1.6 mg/mL of collagen, 16 mM of HEPES, and diluted in DMEM. The pH is adjusted to 6.5 with a 1 M NaOH solution.

The gelling bath is composed of 1 wt% of calcium chloride buffered in 200mM HEPES at pH=7.2, 264 mosmol, and filtered at 0.2 μm. The hydrogel capsules containing cells are produced at a rate around 500 capsules/s and collected during a couple of minutes. The collecting time is small enough for limiting cell sedimentation and thus cell concentration variation during encapsulation. Stirring the cell suspension inside the syringe would then be required for long experiments. They are then filtered out from the gelling solution (Tamis cell strainer 70-100 μm pore size, Fisher Scientific), followed by a washing step with 200 mM HEPES and finally stored in HEPES/Sorbitol solution.

The viability of the encapsulated cells is determined by using a Live/Dead Viability/Cytotoxicity Kit with calcein-AM (CAM, Sigma Aldrich) indicating living cells (green-signal) and propidium iodide for indicating dead cells (red signal). The stained cells inside the capsules are imaged using a Nikon Ti confocal microscope with a 10x objective.

The cell encapsulation experiments have been performed two times for most of the reported conditions. Between 5 and 100 capsules were imaged for each experiment.

Acknowledgements

We thank Danijela Vignevic for having provided us with CT26 cells, SIMM and MMC groups from ESPCI for having given us access to their rheometers and Moshen Dahesh for valuable discussion on rheology. This work was supported by Grant ANR-10-BLAN-1514 from Agence Nationale de la Recherche, France.

References

1 E. R. Shamir and A. J. Ewald, *Nat Rev Mol Cell Biol*, 2014, **15**, 647–664.

2 B. M. Baker and C. S. Chen, *J. Cell Sci.*, 2012, **125**, 3015–3024.

3 L. G. Griffith and M. A. Swartz, *Nat. Rev. Mol. Cell Biol.*, 2006, **7**, 211–224.

4 S. Breslin and L. O'Driscoll, *Drug Discov. Today*, 2013, **18**, 240–249.

5 E. Fennema, N. Rivron, J. Rouwkema, C. van Blitterswijk and J. de Boer, *Trends Biotechnol.*, 2013, **31**, 108–115.

6 F. Hirschhaeuser, H. Menne, C. Dittfeld, J. West, W. Mueller-Klieser and L. A. Kunz-Schughart, *J. Biotechnol.*, 2010, **148**, 3–15.

7 L.-B. Weiswald, D. Bellet and V. Dangles-Marie, *Neoplasia*, 2015, **17**, 1–15.

8 M. Rimann and U. Graf-Hausner, *Curr. Opinion Biotech.*, 2012, **23**, 803–809.

9 H. Uludag, P. De Vos and P. A. Tresco, *Adv. Drug Delivery Rev.*, 2000, **42**, 29–64.

10 G. Orive, E. Santos, D. Poncelet, R. M. Hernández, J. Pedraz, L. U. Wahlberg, P. De Vos and D. Emerich, *Trends Pharmacol. Sci.*, 2015, **36**, 537–546.

11 G. Orive, R. M. Hernandez, A. R. Gascon, R. Calafiore, T. M. S. Chang, P. de Vos, G. Hortelano, D. Hunkeler, I. Lacik and J. L. Pedraz, *Trends Biotechnol.*, 2004, **22**, 87–92.

12 D. Poncelet, R. Lencki, C. Beaulieu, J. P. Halle, R. J. Neufeld and A. Fournier, *Appl. Microbiol. Biotechnol.*, 1992, **38**, 39–45.

13 U. Prusse, L. Bilancetti, M. Bucko, B. Bugarski, J. Bukowski, P. Gemeiner, D. Lewinska, V. Manojlovic, B. Massart, C. Nastruzzi, V. Nedovic, D. Poncelet, S. Siebenhaar, L. Tobler, A. Tosi, A. Vikartovska and K. D. Vorlop, *Chem. Pap.*, 2008, **62**, 364–374.

14 F. Lim and A. Sun, *Science*, 1980, **210**, 908–910.

15 V. Breguet, R. Gugerli, M. Pernetti, U. von Stockar and I. W. Marison, *Langmuir*, 2005, **21**, 9764–9772.

16 S. Sakai, S. Ito and K. Kawakami, *Acta Biomater.*, 2010, **6**, 3132–3137.

17 T. Wang, I. Lacik, M. Brissova, A. V. Anilkumar, A. Prokop, D. Hunkeler, R. Green, K. Shahrokhi and A. C. Powers, *Nat. Biotechnol.*, 1997, **15**, 358–362.

18 M. V. Sefton, R. M. Dawson, R. L. Broughton, J. Blysniuk and M. E. Sugamori, *Biotechnol. Bioeng.*, 1987, **29**, 1135–1143.

19 C. Berkland, E. Pollauf, N. Varde, D. Pack and K. K. Kim, *Pharmaceutical Research*, 2007, **24**, 1007–1013.

20 I. G. Loscertales, A. Barrero, I. Guerrero, R. Cortijo, M. Marquez and A. M. Ganan-Calvo, *Science*, 2002, **295**, 1695–1698.

21 S. Zhao, P. Agarwal, W. Rao, H. Huang, R. Zhang, Z. Liu, J. Yu, N. Weisleder, W. Zhang and X. He, *Integr. Biol.*, 2014, **6**, 874–884.

22 D. Serp, E. Cantana, C. Heinzen, U. von Stockar and I. W. Marison, *Biotechnol. Bioeng.*, 2000, **70**, 41–53.

23 M. Whelehan and I. W. Marison, *J. Microencapsul.*, 2011, **28**,

669–688.
24 C. Berkland, K. K. Kim and D. W. Pack, *J. Controlled Release*, 2001, **73**, 59–74.
25 H. Zhang, E. Tumarkin, R. Peerani, Z. Nie, R. M. A. Sullan, G. C. Walker and E. Kumacheva, *J. Am. Chem. Soc.*, 2006, **128**, 12205–12210.
26 W. Wang, X. D. Liu, Y. B. Xie, H. Zhang, W. T. Yu, Y. Xiong, W. Y. Xie and X. J. Ma, *J. Mater. Chem.*, 2006, **16**, 3252–3267.
27 W. H. Tan and S. Takeuchi, *Adv. Mater.*, 2007, **19**, 2696–2701.
28 L. F. Yu, M. C. W. Chen and K. C. Cheung, *Lab On A Chip*, 2010, **10**, 2424–2432.
29 S. Utech, R. Prodanovic, A. S. Mao, R. Ostafe, D. J. Mooney and D. A. Weitz, *Adv. Healthcare Mater.*, 2015, **4**, 1628–1633.
30 D. Velasco, E. Tumarkin and E. Kumacheva, *Small*, 2012, **8**, 1633–1642.
31 Y. Morimoto, W. H. Tan, Y. Tsuda and S. Takeuchi, *Lab Chip*, 2009, **9**, 2217–2223.
32 C. Kim, S. Chung, Y. E. Kim, K. S. Lee, S. H. Lee, K. W. Oh and J. Y. Kang, *Lab Chip*, 2011, **11**, 246–252.
33 Q. S. Chen, S. Utech, D. Chen, R. Prodanovic, J. M. Lin and D. A. Weitz, *Lab Chip*, 2016, **16**, 1346–1349.
34 N. Bremond, E. Santanach-Carreras, L. Y. Chu and J. Bibette, *Soft Matter*, 2010, **6**, 2484–2488.
35 K. Alessandri, B. R. Sarangi, V. V. Gurchenkov, B. Sinha, T. R. Kiessling, L. Fetler, F. Rico, S. Scheuring, C. Lamaze, A. Simon, S. Geraldo, D. Vignjevic, H. Domejean, L. Rolland, A. Funfak, J. Bibette, N. Bremond and P. Nassoy, *Proc. Natl. Acad. Sci. USA*, 2013, **110**, 14843–14848.
36 C. Clanet and J. C. Lasheras, *J. Fluid Mech.*, 1999, **383**, 307–326.
37 X. Zhang and O. A. Basaran, *Phys. Fluids*, 1995, **7**, 1184–1203.
38 A. V. Anilkumar, I. Lacik and T. G. Wang, *Biotechnol. Bioeng.*, 2001, **75**, 581–589.
39 J. Eggers and E. Villermaux, *Rep. Prog. Phys.*, 2008, **71**, 036601.
40 E. F. Goedde and M. C. Yuen, *J. Fluid Mech.*, 1970, **40**, 495–511.
41 H. Brandenberger, D. Nüssli, V. Piëch and F. Widmer, *J. Electrostat.*, 1999, **45**, 227–238.
42 J. M. Schneider, N. R. Lindblad, J. C. D. Hendricks and J. M. Crowley, *J. Appl. Phys.*, 1967, **38**, 2599–2605.
43 E. J. Hinch, O. J. Harris and J. M. Rallison, *J. Non-Newtonian Fluid Mech.*, 1992, **43**, 311–324.
44 R. Govindarajan and K. C. Sahu, *Annu. Rev. Fluid Mech.*, 2014, **46**, 331–353.
45 N. B. Wyatt and M. W. Liberatore, *Soft Matter*, 2010, **6**, 3346–3352.
46 M. Rubinstein and R. H. Colby, *Polymer physics*, Oxford Univ Press, 2008.
47 R. I. Tanner, *J. Polym. Sci. A-2 Polym. Phys.*, 1970, **8**, 2067–2078.
48 C. Allain, M. Cloitre and P. Perrot, *J. Non-Newtonian Fluid Mech.*, 1997, **73**, 51–66.
49 S. L. Goren and S. Wronski, *J. Fluid Mech.*, 1966, **25**, 185–198.
50 H. Doméjean, J. Bibette and N. Bremond, *Phys. Rev. Fluids*, 2016 **1**, 063903.
51 L. Rolland, E. Santanach-Carreras, T. Delmas, J. Bibette and N. Bremond, *Soft Matter*, 2014, **10**, 9668–9674.
52 S. Chandrasekhar, *Rev. Mod. Phys.*, 1943, **15**, 0001–0089.
53 J. M. Kelm, N. E. Timmins, C. J. Brown, M. Fussenegger and L. K. Nielsen, *Biotechnol. Bioeng.*, 2003, **83**, 173–180.
54 M. D. Ungrin, C. Joshi, A. Nica, C. Bauwens and P. W. Zandstra, *PLoS ONE*, 2008, **3**, e1565.
55 R. Glicklis, J. C. Merchuk and S. Cohen, *Biotechnol. Bioeng.*, 2004, **86**, 672–680.
56 E. Curcio, S. Salerno, G. Barbieri, L. De Bartolo, E. Drioli and A. Bader, *Biomaterials*, 2007, **28**, 5487–5497.
57 J. A. Rowley, G. Madlambayan and D. J. Mooney, *Biomaterials*, 1999, **20**, 45–53.
58 K. Y. Lee and D. J. Mooney, *Prog. Polym. Sci.*, 2012, **37**, 106–126.
59 J. Venkatesan, I. Bhatnagar, P. Manivasagan, K.-H. Kang and S.-K. Kim, *Int. J. Biol. Macromolec.*, 2015, **72**, 269–281.
60 K. Alessandri, M. Feyeux, B. Gurchenkov, C. Delgado, A. Trushko, K. H. Krause, D. Vignjevic, P. Nassoy and A. Roux, *Lab Chip*, 2016, **16**, 1593–1604.
61 A. Funfak, N. Atrux-Tallau, N. Bremond and J. Bibette, *To be submitted*.
62 L. Baraban, F. Bertholle, M. L. M. Salverda, N. Bremond, P. Panizza, J. Baudry, J. A. G. M. de Visser and J. Bibette, *Lab Chip*, 2011, **11**, 4057–4062.
63 L. Boitard, D. Cottinet, N. Bremond, J. Baudry and J. Bibette, *Eng. Life Sci.*, 2015, **15**, 318–326.
64 H. Doméjean, *PhD thesis*, UPMC, 2014.